Progress toward a microradiation therapy small animal conformal irradiator

Strahinja Stojadinovic, Daniel A. Low, Milos Vicic, Sasa Mutic, Joseph O. Deasy, Andrew J. Hope, Parag J. Parikh, and Perry W. Grigsby
Washington University School of Medicine, St. Louis, Missouri 63110

Microradiation therapy (microRT) systems are being designed to provide conformal radiation therapy to small animals enabling quantitative radiation response evaluation. We used a Monte Carlo approach to estimate the radiation dose distributions from proposed blueprints and developed a beam model to aid in the microRT system design process. This process was applied to a prototype irradiator that uses a small (3 mm long and 3 mm in diameter), cylindrical, high-activity ^{192}Ir source delivering the radiation beam using custom-fabricated tungsten collimators. The BEAMnrc Monte Carlo code was used to simulate dose distributions from these prototype collimators. Simulations were performed at three source-to-surface distances (50, 60, and 70 mm), and with five circular field sizes (5, 7.5, 10, 12.5, and 15 mm). A dose to a $50 \times 50 \times 50$ mm^3 water phantom with $1 \times 1 \times 1$ mm^3 voxel spacing was computed. A multiparameter dose calculation algorithm was developed to efficiently and accurately calculate doses for treatment planning exercises. The parametrization was selected so that the parameters varied smoothly as a function of depth, source-to-surface distance, and field size, allowing interpolation for geometries that were not simulated using the Monte Carlo simulation. Direct comparison of the model with the Monte Carlo simulations showed that the variations were within 5% error for field sizes larger than 10 mm, and up to 10% for smaller field sizes. © *2006 American Association of Physicists in Medicine*.
[DOI: 10.1118/1.2349693]

Key words: microRT, small animal radiation therapy, beam model, Monte Carlo simulations, 3D dose distribution

I. INTRODUCTION

Animal models are essential for improving cancer detection and functional characterization and provide a framework to develop and validate cancer therapies. Most current research evaluating therapeutic response has been focused toward chemotherapeutic agents. While radiation therapy is an important therapeutic modality in humans, animal experimentation is limited because the current technology of animal irradiation is nonconformal, making selective irradiation of *in situ* tumors and normal organs difficult. The majority of small-animal radiation-therapy studies involve the irradiation of implanted tumors, either on the animal's back or hindquarters.[1] Typical implanted tumor sizes in nude mice range from 100 to 1500 mm^3, corresponding to a projected cross-sectional field size of 5.8–14.2 mm diam, respectively. Limited numbers of studies have used animal models to investigate normal-tissue radiation sensitivity, most involving whole-animal irradiation.[2] Conformal animal irradiation studies are scarce. Khan *et al.*[3,4] recently conducted partial-lung irradiation on Sprague-Dawley rats, exposing them to doses up to 20 Gy using ^{60}Co. They used a clinical total body irradiation unit and 10 cm thick lead blocks to define the irradiation fields. The limitations of such technique are abundant. A modified gamma knife was used as more sophisticated small animal irradiator. For example DesRosiers *et al.*[5] and references therein used the stereotactic technique for irradiating rodents.

A small animal conformal irradiator or a microradiation therapy (microRT) device is a missing link for studying response to therapeutic doses of radiation. [To distinguish between human and animal use, systems developed for small animal imaging typically have the prefix "micro" added to the imaging acronym. These newly developed devices include microcomputed tomography (microCT), micropositron emission tomography (microPET), micromagnetic resonance (microMR), and, more recently, micro-single-photon-emission computed tomography (microSPECT). We use the same convention for our small animal irradiator, microRT.] A microRT device should provide accurate spatial registration of the animal's internal anatomy and the radiation beam. This can be accomplished by visual methods, palpation, alignment with rigid head structures such as the ear canals and mouth, or by image guidance. The flexible nature of a mouse or rat skin makes the use of skin marks impractical in the thorax, abdomen, or pelvis regions. Along with the alignment method, the radiation beam characteristics will be critical to the success of the irradiator. We are designing an irradiator for mice and rats with variable source-to-target distance (STD) and collimator opening providing desired depth dose and beam divergence at the target. The irradiator will use a radioisotope, rather than a kilovoltage x-ray unit, as the radiation source. The principal advantage of using a radioactive source is estimated reduced equipment cost and reduced technical complexity. The primary disadvantages of using a
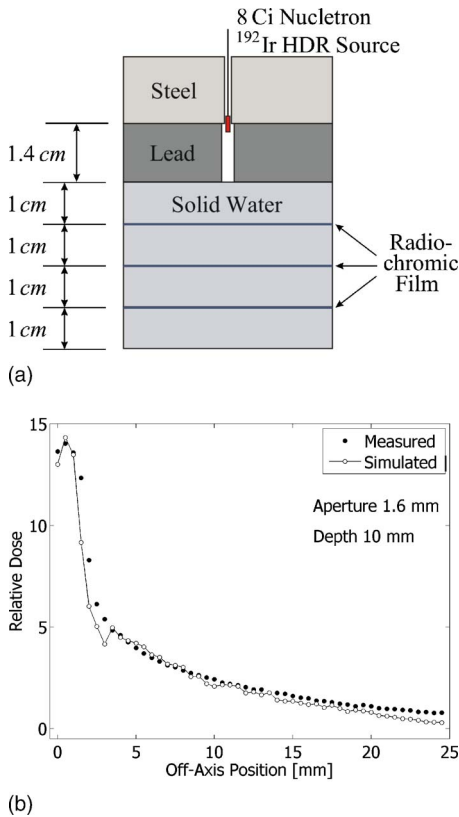
FIG. 1. (a) Experimental setup used for validation of Monte Carlo computations. (b) Radial profile for 1.6 mm aperture shows good agreement between Monte Carlo data and radiochromic film measurements.

FIG. 2. Collimator prototype for a small animal radiation therapy device.

radioisotope are the inability to shut off the radiation, the requirement for source replacement, and the greater shielding requirements.

To improve the dose distribution characteristics in tissues, we selected ^{192}Ir, a higher-energy radioisotope source with a high specific activity and mass density. ^{192}Ir decays by β^- (95.3%) to ^{192}Pt and by electron capture (4.7%) to ^{192}Os. The β^- energy spectrum[6] ranges from 22.5 to 667.5 keV, making shielding of the β^- straightforward. The ^{192}Ir gamma spectrum[6] ranges from 7 to 885 keV with an average energy of 380 keV.

A previous study[7] showed that in water, from 1.5 to 6 cm STD, the depth dose was dominated by the inverse-square component for gamma rays greater than 100 keV. This preceding work compared Monte Carlo simulations of a Nucletron HDR ^{192}Ir source with corresponding radiochromic film measurements for various circular collimator openings (see Fig. 1).

The goal of the Monte Carlo simulations presented in this article was to guide our microRT hardware design and provide a base for the development of treatment planning software. For this initial implementation, the dosimetric and spatial precision goals were 5% and 1 mm, respectively. The spatial resolution of the study was limited to 1 mm to allow a relatively large number of simulations, and is within the intended precision. This article is concerned primarily with the implementation of a beam model for dose distribution
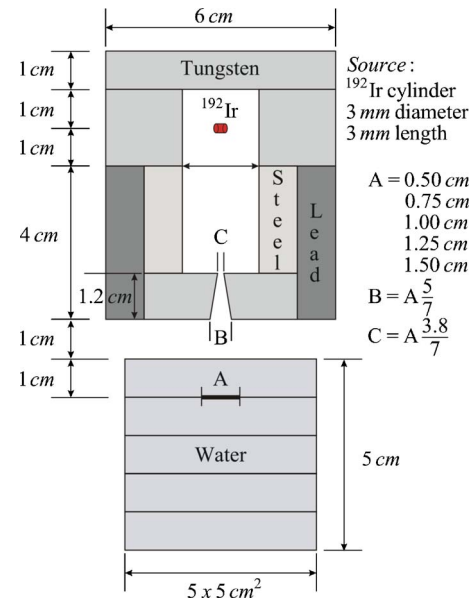
simulations and presents a further development of the ideas and results presented at international conference proceedings.[7]

II. MATERIALS AND METHODS

A. Monte Carlo calculations

The BEAMnrc[8] Monte Carlo simulation code, with an incorporated EGSnrc[9] engine, was used to evaluate the impact of source size, collimation material and geometry, and source-to-target distance on the resulting radiation dose distribution, and provide input data for and validate the microRT dose calculation algorithm. The code has various geometry modeling features that make it convenient for use in collimator prototype evaluations.

There were two steps in performing Monte Carlo simulations. The first was to model the source within a prototype collimator, then generate particles from the source and form a phase-space file that contains the particles' energies and momenta. The second step was to direct the particles from the phase-space file into a water phantom and compute a three-dimensional (3D) dose distribution.

As stated above, the first step in the simulation was to model a prototype collimator and source, which was done with the BEAMnrc Graphical User Interface (BEAM_GUI). A high-activity 3 mm diam, 3 mm long right cylinder of ^{192}Ir was selected as the source to be simulated and used in the prototype irradiator. The energy distribution of the initial photons from the ^{192}Ir radionuclide was taken from Duchemin and Coursol.[6] The electron beam from the source was ignored since it only contributes to a surface dose for β^- spectral energies of ^{192}Ir. The built-in photon mass energy absorption coefficients in the BEAMnrc code were used for photon transport in various media. Photon transport within the source, i.e., self-shielding of the source, was also taken into account. This was done by matching the simulated cy-

TABLE I. The summary of Monte Carlo EGSnrc parameters used for generating phase space files.

Monte Carlo EGSnrc Transport Parameters			
Maximum step size (cm):	default	Bremsstrahlung angular sampling:	simple
Maximum fractional energy loss/step:	default	Bremsstrahlung cross sections:	Bethe-Heitler
Maximum first elastic scattering moment/step:	default	Bound Compton scattering:	Klein-Nishina
Boundary crossing algorithm:	PRESTA-I	Pair angular sampling:	simple
Skin depth:	0	Photoelectron angular sampling:	off
Electron-step algorithm:	PRESTA-II	Rayleigh scattering:	off
Spin effects:	on	Atomic relaxations:	off

lindrical geometry of the source with a uniform isotropically radiating internal ^{192}Ir core of the same geometry. The source was not encapsulated in the simulations. This small-size, high-activity ^{192}Ir source was positioned within a conical aperture tungsten collimator, as shown in Fig. 2. The collimator and cylindrical source axes of symmetry were set to be mutually perpendicular in the simulations, i.e., the cylindrical surface of the source was facing the collimator opening.

The summary of Monte Carlo EGSnrc transport parameters used for generating radiation beams, i.e., phase-space files with the particles' energies and momenta, is given in Table I. Circular fields defined at 10 mm phantom depth were simulated with field size (FS) diameters in steps of 2.5 mm from 5 to 15 mm. The total number of histories per simulation was 24×10^9. Only a fraction of this number of particles passed through the variable collimator opening, denoted by C, and predetermined by the desired field size A, illustrated in Fig. 2, to form the phase space file. For example, for the 15 mm diam field size at a 60 mm source-to-surface distance, the number of particles in the phase-space file was 55×10^6. The phase-space files were generated for each collimator and subsequently used in simulations for three source-to-surface distances (SSDs): 50, 60, and 70 mm, corresponding to 0, 10, and 20 mm air gaps between the collimator face and phantom. For each SSD there were five simulated field sizes, bringing the total number of performed simulations to 15. Figure 2 shows the 60 mm SSD, which was selected as the reference SSD (SSD_{ref}).

The next step in the simulation task was to compute the 3D dose distribution using the precomputed phase-space files. A $50 \times 50 \times 50$ mm^3 water phantom was simulated with $1 \times 1 \times 1$ mm^3 voxels. For this purpose the DOSXYZnrc Graphical User Interface (DOSXYZnrc_GUI) was used and some of the Monte Carlo parameters were changed to improve the dose scoring accuracy. For example, in addition to all other parameter settings previously used for particle generation, the boundary crossing algorithm was set to be "exact," the bremsstrahlung cross sections were used from the NIST database, and atomic relaxations and photoelectron angular sampling were turned "on." Due to practical considerations of generating the phase-space files, the phase-space particles were recycled for the 3D dose distribution simulations. The photons from a phase-space file were recycled up to 25 times.

B. Dose modeling

It is known from literature[10] that a general 3D dose distribution can be written in a canonical form. The advantage of the canonical form is having a dose distribution reduced to its components without loss of generality. The proposed canonical formula for the purposes of this paper includes the following elements:

$$3D \text{ dose} = D_{ref} \times PDD \times ISF \times OF \times OAF, \quad (1)$$

where

$$D_{ref} = \text{dose(at central axis, } SSD_{ref}, FS_{ref}, \text{ and } d_{ref}), \quad (2)$$

$$PDD = \left[\frac{\text{dose (at given depth } d)}{\text{dose(at reference depth } d_{ref})} \right]_{\text{at central axis, } SSD_{ref}, \text{ and } FS_{ref}}, \quad (3)$$

$$ISF = \left[\frac{SSD + d_{ref}}{SSD + d} \right]^2, \quad (4)$$

$$OF = \left[\frac{\text{dose(at given field size FS)}}{\text{dose(at reference field size } FS_{ref})} \right]_{\text{at central axis, } SSD_{ref}, \text{ and } d_{ref}}, \quad (5)$$

$$OAF = \left[\frac{\text{dose(at off-axis distance)}}{\text{dose(at central axis)}} \right]_{\text{at given SSD and FS}}. \quad (6)$$
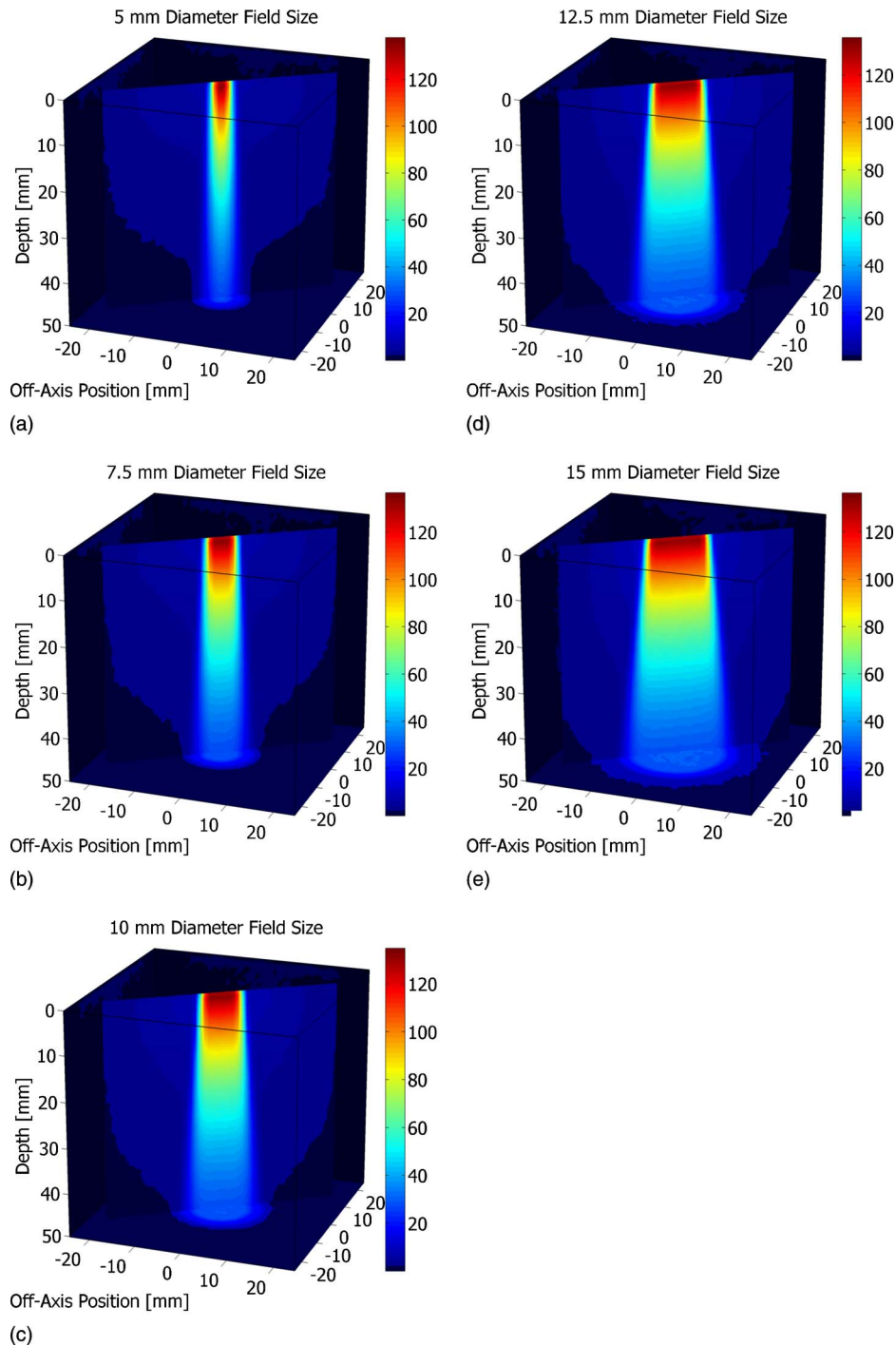
FIG. 3. Normalized beam profiles for various collimator openings at the reference source-to-surface distance $SSD_{ref}=60$ mm corresponding to (a) 5, (b) 7.5, (c) 10, (d) 12.5, and (e) 15 mm diam field size at the reference depth $d_{ref}=10$ mm.

Here, D_{ref} is the reference dose at the beam central axis, at the reference SSD, SSD_{ref}, at the reference field size FS_{ref}, and at the reference depth d_{ref}. For purposes of these simulations, the reference values were selected to be $SSD_{ref}=60$ mm, $FS_{ref}=10$ mm, and $d_{ref}=10$ mm. The percent depth dose PDD is defined as the ratio of dose at the central axis at depth d with the dose at the central axis at the reference depth d_{ref}, but without the inverse square attenuation. ISF is the inverse-square factor defined as the square of the ratio of

distance between the source and the reference point, i.e., $SSD+d_{ref}$, and the distance between the source and the calculation point, $SSD+d$. The output factor OF is defined as the dose at the central axis at the reference depth d_{ref} for the given field size FS divided by the dose at central axis at d_{ref} for the reference field size FS_{ref}. The off-axis factor OAF represents a dose profile and changes as the dose changes due to off-axis displacement. OAF is defined as the ratio of

the dose at the off-axis distance and the dose at the central axis, for given SSDs and FSs.

Finding a function that will adequately represent a dose profile, i.e., OAF, is essential. A double Boltzmann function was used to represent the dose profiles:

$$y(x) = \frac{A_1}{1 + \exp\left(\dfrac{x - x_{01}}{\Delta x_1}\right)} + \frac{1 - A_1}{1 + \exp\left(\dfrac{x - x_{02}}{\Delta x_2}\right)}. \tag{7}$$

The double Boltzmann function produces a sigmoidal curve with a tail in the base and utilizes five parameters that can be varied: A_1, x_{01}, Δx_1, x_{02}, and Δx_2. The first term depicts beam profiles formed from particles passed through the collimator opening and the second one encompasses the tail of the beam and the background radiation formed by particles that passed through the collimator walls.

The obtained Monte Carlo 3D dose distributions were separated into radial and depth dependences. Radial profiles were fit to the double Boltzmann function. After the inverse-square behavior was factored out, the attenuation with depth was depicted by a quadratic function. The fit parameters were then used to regenerate 3D dose distributions, which were compared to the Monte Carlo results. Ultimately, 3D dose distributions were represented in the canonical form in order to be able to predict distributions in regions that were not simulated. Lastly, the model and Monte Carlo results were intercompared using dose differences and the gamma method.[11]

The proposed dose calculation algorithm [Eq. (1)] was compared against previously validated Monte Carlo dose calculations.[7] This preceding work compared Monte Carlo simulations of a Nucletron HDR ^{192}Ir source with corresponding radiochromic film measurements for various circular collimator openings. The experimental setup and the comparison between simulated and measured values for a 1.6 mm diam aperture are shown in Fig. 1. The radiochromic film measurements were made in accordance with the protocol suggested by Dempsey *et al.*[12] Radiochromic film sheets (5 cm × 5 cm) were placed between 1.0 cm thick water-equivalent phantom material and irradiated to a maximum of 15 Gy. Monte Carlo simulations were conducted for the same geometry and compared against the radiochromic film measurements. The Monte Carlo simulation data was normalized such that the average dose within the collimator opening (excluding the centralmost point) was equal. The dose distribution was binned in radial increments of 0.5 mm, as shown in Fig. 1(b). The centralmost point was typically a few percent lower than the rest of the collimator opening. The dip in the centralmost point is a consequence of vertical or "end-on" orientation of the source, since the self-absorption of the source increases at the end point due to the thickest shielding of the steel capsule. Figure 1(b) shows that the simulation and measurement agreed within the collimator opening and penumbra (out to 2.0 cm radius) to within 5% of the maximum dose and within 0.5 mm in the steep dose gradient regions. One point in Fig. 1(b) exceeds the 5%, 0.5 mm comparison, and is assumed to be due to statistical variation.
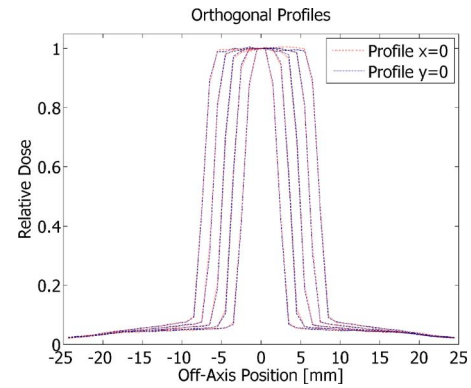
FIG. 4. Radial symmetry of beam profiles for five different field sizes at the reference source-to-surface distance $\text{SSD}_\text{ref} = 60$ mm.

III. RESULTS

Selected planar samples through the 3D dose distributions are shown in Fig. 3. They correspond to five field sizes at 60 mm reference source-to-surface distance SSD_ref, normalized at a reference depth d_ref of 10 mm. The statistical uncertainty of the computed Monte Carlo dose distributions along the central axis was ±0.8% on average.

In megavoltage radiation therapy, the buildup region or the depth of maximum dose (d_max) is generally known to depend on field size as well as on the SSD; d_max tends to decrease with decreasing field size and increase with increasing SSD. The skin sparing caused by secondary electron buildup may be less important for animal experiments than for human irradiation, but reducing the discomfort and potential for infection caused by skin overirradiation may be important for some animal experiments. To test this and to determine d_max for the ^{192}Ir photons, d_max was determined by examining depth-dose distributions. Plotting d_max as a function of field size showed that d_max was less than 1.5 mm. The reference depth d_ref had to be equal or greater than d_max, and in this analysis it was chosen to be at 10 mm.

The geometry of the source, its orientation with respect to the collimator, and SSD are factors in forming dose profiles. The collimator and cylindrical source axes of symmetry were set to be mutually perpendicular in the simulations. It was
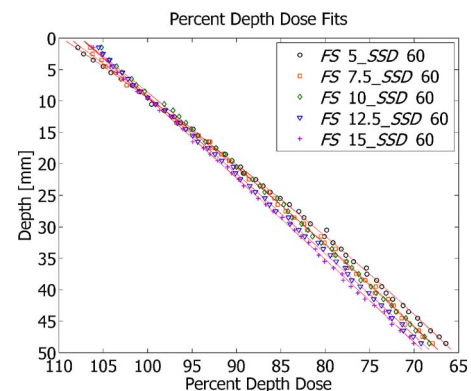

FIG. 5. Percent depth dose attenuation for five field sizes at the reference source-to-surface distance $\text{SSD}_\text{ref} = 60$ mm.
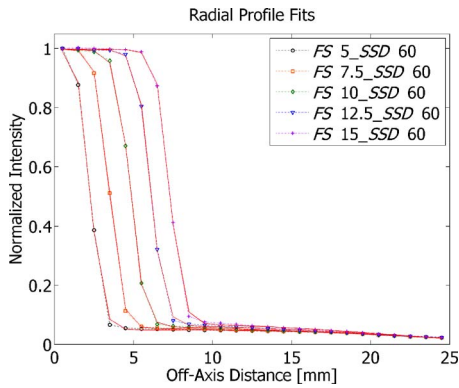
FIG. 6. Normalized beam profiles and the corresponding radial fits for five field sizes at the reference source-to-surface distance $SSD_{ref}=60$ mm.

FIG. 8. Normalized and scaled radial profile fits for the reference field size $FS_{ref}=10$ mm and source-to-surface distance $SSD_{ref}=60$ mm.

anticipated that this orientation and the geometry of the source would produce dose distributions with asymmetric penumbrae. Because the source size was small relative to the target distance, the asymmetry was found to be small, about 10% in the steepest (penumbra) region. Figure 4 shows two superimposed orthogonal profiles at 10 mm depth (dotted and dashed lines), used to check the asymmetry of the dose distributions for different field sizes. For purposes of dose modeling, the beams were considered radially symmetric.

After the inverse-square attenuation of the beams was removed, the resulting normalized depth-dose distributions were fit to a second-order polynomial function. The Monte Carlo simulation data for SSD_{ref} are shown in various symbols, each corresponding to five different field sizes, and the depth-dose fits are represented as solid lines in Fig. 5. The buildup region (<1.5 mm) was ignored for this analysis.

Radial profiles, normalized at the central axis, were fit to the double Boltzmann function, given by Eq. (7). Figure 6 shows the profiles for a simulation corresponding to SSD_{ref}. The Monte Carlo radial distributions are shown as dashed lines and the radial fits are shown as solid lines.

The fit function has five independent parameters. The behavior of the parameters was modeled as a function of phantom depth and field size using the 60 mm SSD as SSD_{ref} and the 10 mm reference field size. For each scoring plane along

the central axis, a depth-dose profile was generated, resulting in 50 profiles. The decrease in dose with increased depth governed by the inverse-square law was removed, all profiles were normalized at a reference depth of 10 mm, and in addition to that, the off-axis distance scale was renormalized to remove the geometric divergence (see Fig. 7). These normalized and scaled profiles were then fit to the double Boltzmann function given by Eq. (7). The resulting normalized and scaled profile fits are shown in Fig. 8. The error between radial profiles and radial profile fits was less than 3%, as shown in Fig. 9, even in the steep dose gradient regions, indicating that the double Boltzmann fitting function was capable of accurately reproducing the profile shapes.

In order to compare the fits to the Monte Carlo generated data, the 3D dose distributions were computed using the following procedure. From the known sets of fit parameters (A_1, x_{01}, Δx_1, x_{02}, and Δx_2) compute the scaled radial profiles for each phantom depth d. Multiply the scaled radial profiles with the percent depth dose PDD to account for phantom attenuation and take into account the inverse square factor ISF to obtain the 3D dose distribution. Hence,
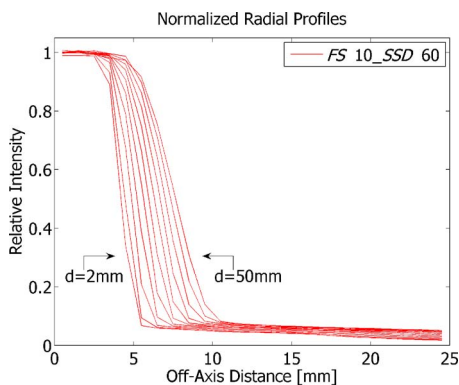

FIG. 7. Depth variation of selected normalized radial profiles (geometric divergence) for the reference field size $FS_{ref}=10$ mm and source-to-surface distance $SSD_{ref}=60$ mm.
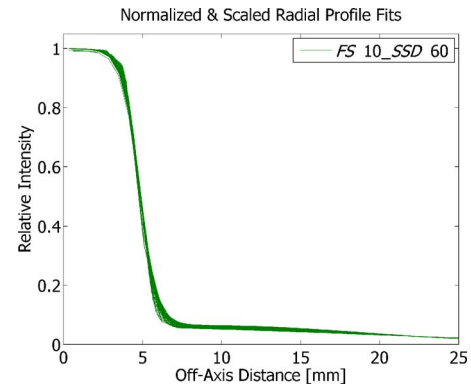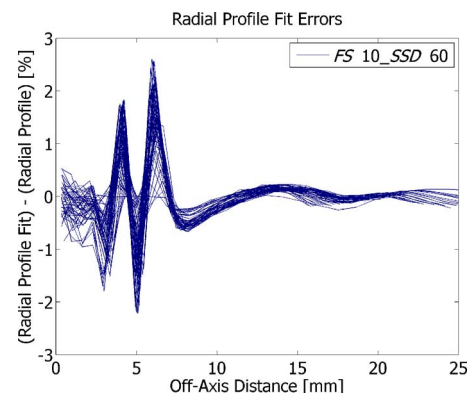

FIG. 9. Radial profile fit errors for the reference field size $FS_{ref}=10$ mm and source-to-surface distance $SSD_{ref}=60$ mm.
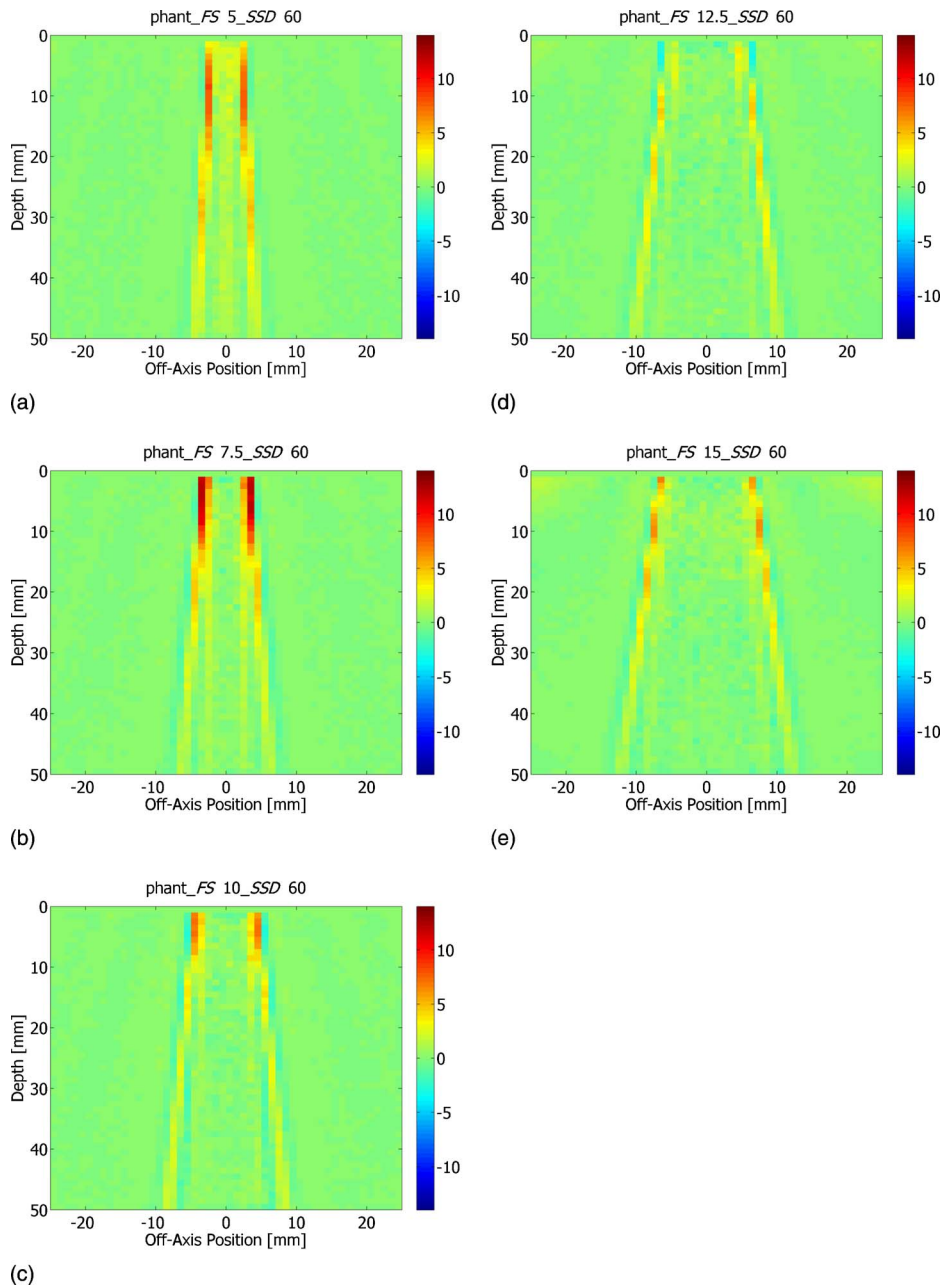
FIG. 10. Differences between Monte Carlo dose distributions and the corresponding fits at the reference source-to-surface distance SSD$_{ref}$=60 mm for five field sizes: FS= (a) 5, (b) 7.5, (c) 10, (d) 12.5, and (e) 15 mm.

3D dose = Radial Profiles × PDD × ISF

$$= \left[\frac{A_1}{1 + \exp\left(\dfrac{r' - x_{01}}{\Delta x_1}\right)} + \frac{1 - A_1}{1 + \exp\left(\dfrac{r' - x_{02}}{\Delta x_2}\right)} \right]$$

$$\times \text{PDD} \times \text{ISF}, \tag{8}$$

where PDD and ISF are given by Eqs. (3) and (4), respectively, and $r' = r(\text{SSD} + d_{ref}/\text{SSD} + d)$ is a scaled radial distance. Examples of dose-difference comparisons are shown in Fig. 10 for the 60 mm SSD case and five field sizes. The dose differences are greater than 5% only in the penumbra regions for small field sizes (<10 mm).

In order to compute dose to arbitrary field sizes and SSDs, the fit parameters were interpolated using a polynomial parameterization. Because of the suitable fit function, the five fit parameters varied smoothly as a function of depth and a function of field size. For each parameter, if plotted simultaneously, this functional dependence on two variables formed a 2D surface (see Fig. 11). Each surface in this instance was represented by the following form:

$$\text{surface} = a_o + a_x X + a_y Y + a_{xy} XY, \tag{9}$$

where X and Y represent depth and field size, respectively, while a_o, a_x, a_y, and a_{xy} are surface fit coefficients. For given SSD$_{ref}$, parameter values (A_1, x_{01}, Δx_1, x_{02}, and Δx_2)

A1 = f (Field Size, Depth)

(a)

FIT A1 = f (Field Size, Depth)

(b)

x01 = f (Field Size, Depth)

(c)

FIT x01 = f (Field Size, Depth)

(d)
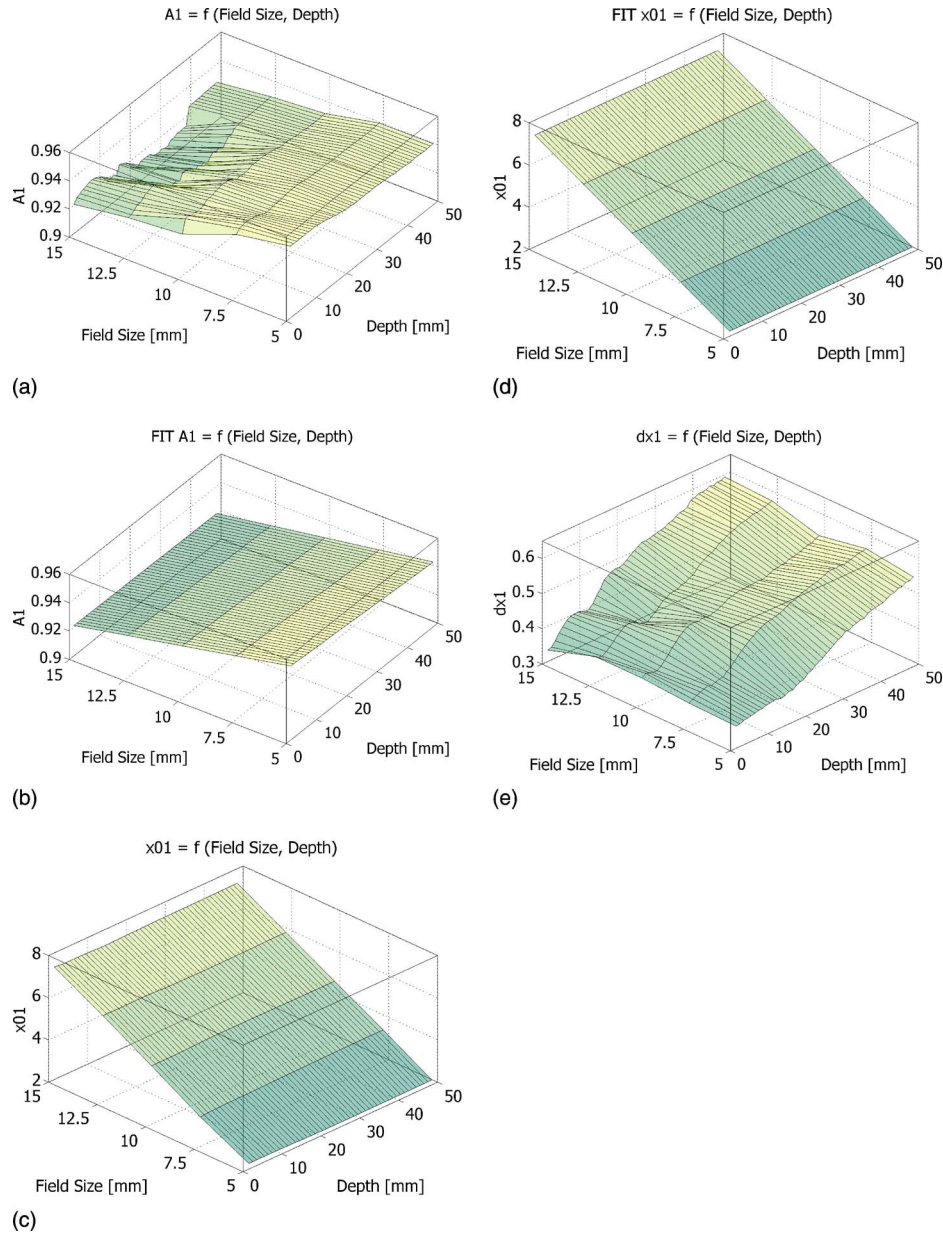
dx1 = f (Field Size, Depth)

(e)

Fig. 11. Field size (FS) and depth (d) dependence of fit parameters and the corresponding surface fits for the reference source-to-surface distance SSD_{ref} =60 mm. (a) $A_1=f(FS,d)$; (b) Fit $A_1=f(FS,d)$; (c) $x_{01}=f(FS,d)$; (d) Fit $x_{01}=f(FS,d)$; (e) $\Delta x_1=f(FS,d)$; (f) Fit $\Delta x_1=f(FS,d)$; (g) $x_{02}=f(FS,d)$; (h) Fit x_{02} $=f(FS,d)$; (i) $x_2=f(FS,d)$; (j) Fit $\Delta x_2=f(FS,d)$.

can be read directly from the corresponding surface fit for any field size and for any depth. If a different SSD is needed, however, the desired parameter values can be obtained by interpolating between $SSD_{ref}=60$ mm and the other two simulated SSDs (50 and 70 mm). This method produced 3D dose distributions that were compared to the Monte Carlo calculated distributions. As an example, the differences between six Monte Carlo dose distributions for field sizes of 5, 10, and 15 mm at 50 and 70 mm SSDs, and the corresponding distributions generated by using Eq. (1) are shown in Fig. 12. For larger field sizes (<10 mm), the differences are within 5% of error, while these differences are somewhat greater, up to 10%, for smaller field sizes.

The model was tested independently by the gamma dose distribution comparison method.[11] The reference and evaluated dose distributions were the simulated Monte Carlo and Eq. (1)-predicted dose distributions, respectively. For comparison purposes, the dose difference and distance-to-agreement criteria were 5% and 1 mm, respectively. The Monte Carlo distribution was considered to be the "reference" distribution, and the evaluated distribution was computed on a 0.25 mm spacing for purposes of computing gamma. As the reference distribution, the relatively coarse Monte Carlo spacing did not affect the gamma calculation accuracy.[11] Figure 13 shows the results of the gamma dose assessment with contours enclosing regions where dose dif-
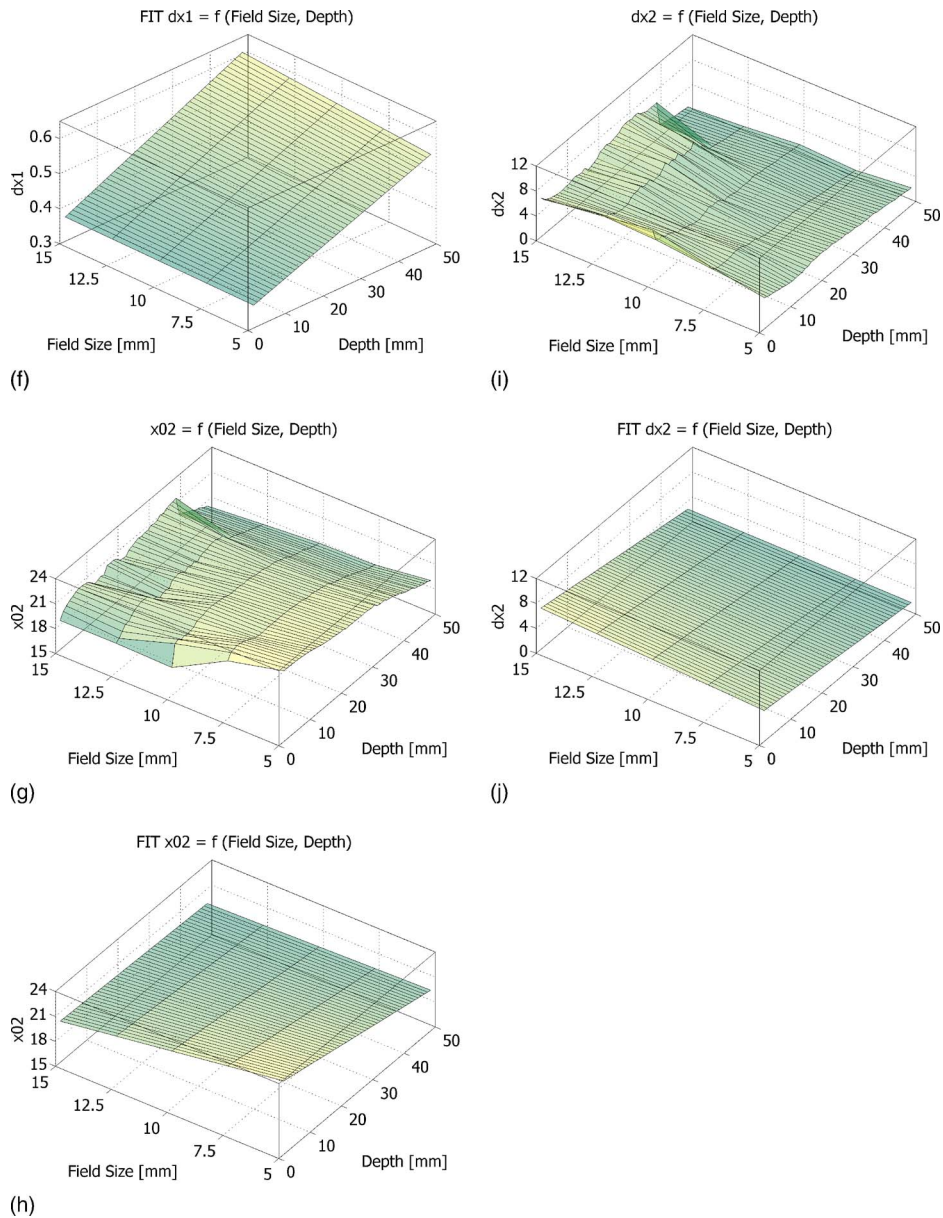
(f)

(i)

(g)

(j)

(h)

Fig. 11. (*Continued*).

ferences are larger than 5%. Thus, the predicted and the Monte Carlo dose distributions differ by less than 5% for field sizes larger than 10 mm, whereas these differences approach 10% for smaller fields only in the shallow phantom regions.

Heterogeneity corrections were not explicitly investigated in this study; they were estimated using the latest XCON: Photon Cross Sections Database[13] from the National Institute of Standards and Technology. The mass attenuation coefficients corresponding to the full ^{192}Ir gamma spectrum[6] were obtained from the online database for water, air (a mixture of 78.09% N_2, 23.95% O_2, 0.93% Ar, and 0.03% CO_2), and bone (calcium phosphate, $Ca_3P_2O_8$). Using the mass attenuation coefficients, weighted according to the corresponding energy fraction of the entire ^{192}Ir photon spectrum, we esti-

mated that the heterogeneity correction for a 2 mm thick bone is about 2.5%, and for a 1 cm lung cavity it is about 15%.

IV. DISCUSSION AND CONCLUSIONS

This paper presents an investigation of a beam model for purposes of a microRT conformal irradiator using an ^{192}Ir source. The simulations were performed using the BEAMnrc code with the EGS4 Monte Carlo engine. We developed a fast dose calculation algorithm that is accurate in water for 3D dose distributions generated by Monte Carlo simulations.

The dose falloff with distance in tissue for ^{192}Ir is practically indistinguishable from the inverse square law up to 5
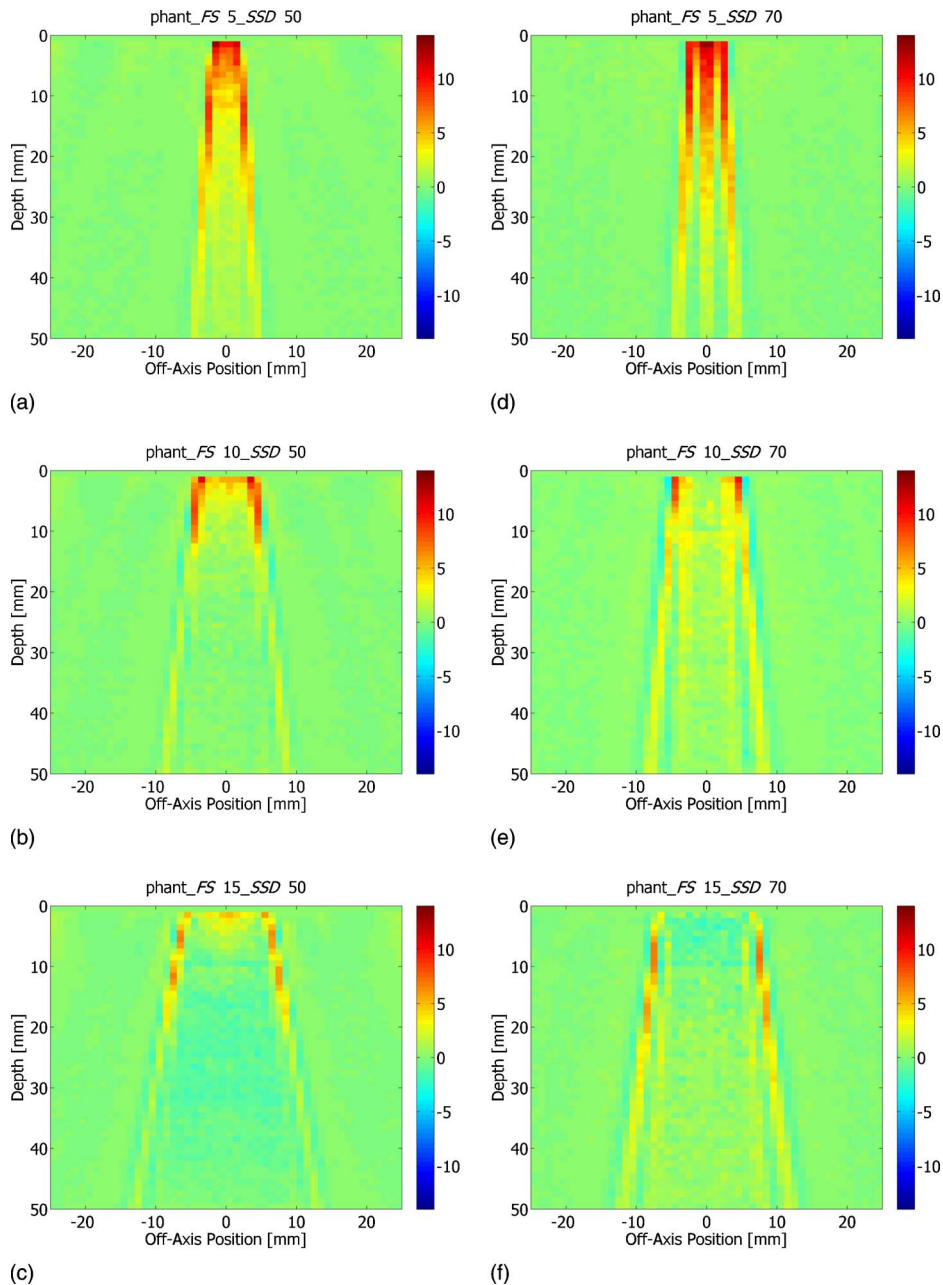
FIG. 12. Differences between dose distributions obtained by the Monte Carlo simulations and the corresponding distributions obtained by using the canonical form. Left column: dose differences for SSD=50 mm and FS= (a) 5, (b) 10, and (c) 15 mm. Right column: dose differences for SSD=70 mm and FS= (d) 5, (e) 10, and (f) 15 mm.

cm.[10] In our hardware design, a beam penetrates relatively small phantom depths. In addition to that, the estimated heterogeneity correction, using the entire ^{192}Ir spectrum for a 2 mm thick bone is about 2.5%, and except for the lung region it is not substantial for mouse and rat irradiation. For accurate treatment planning calculations the heterogeneity corrections can be implemented in the proposed algorithm using standard methods, for instance, tissue-air ratio methods.

The double Boltzmann function, given by Eq. (7), was used to provide representation of the beams' radial profiles. It converged to a solution with the lowest chi-square value when compared to several other exponential fit functions

considered for beam modeling. The five fit parameters (A_1, x_{01}, Δx_1, x_{02}, and Δx_2) vary smoothly with depth and field size. Superimposed orthogonal radial profiles for five field sizes, plotted in Fig. 4, show virtually no anisotropy and for practical purposes may be considered symmetric. However, there is up to 10% asymmetry in penumbra regions, which would be substantially greater for the chosen cylindrical ^{192}Ir source if the SSD is reduced.

Within the scope of simulated Monte Carlo computations, we have shown that a canonical approach can accurately represent and predict 3D dose distributions in a homogeneous water phantom. For distributions that are outside of the simulated domain, extrapolation methods can be used. However,
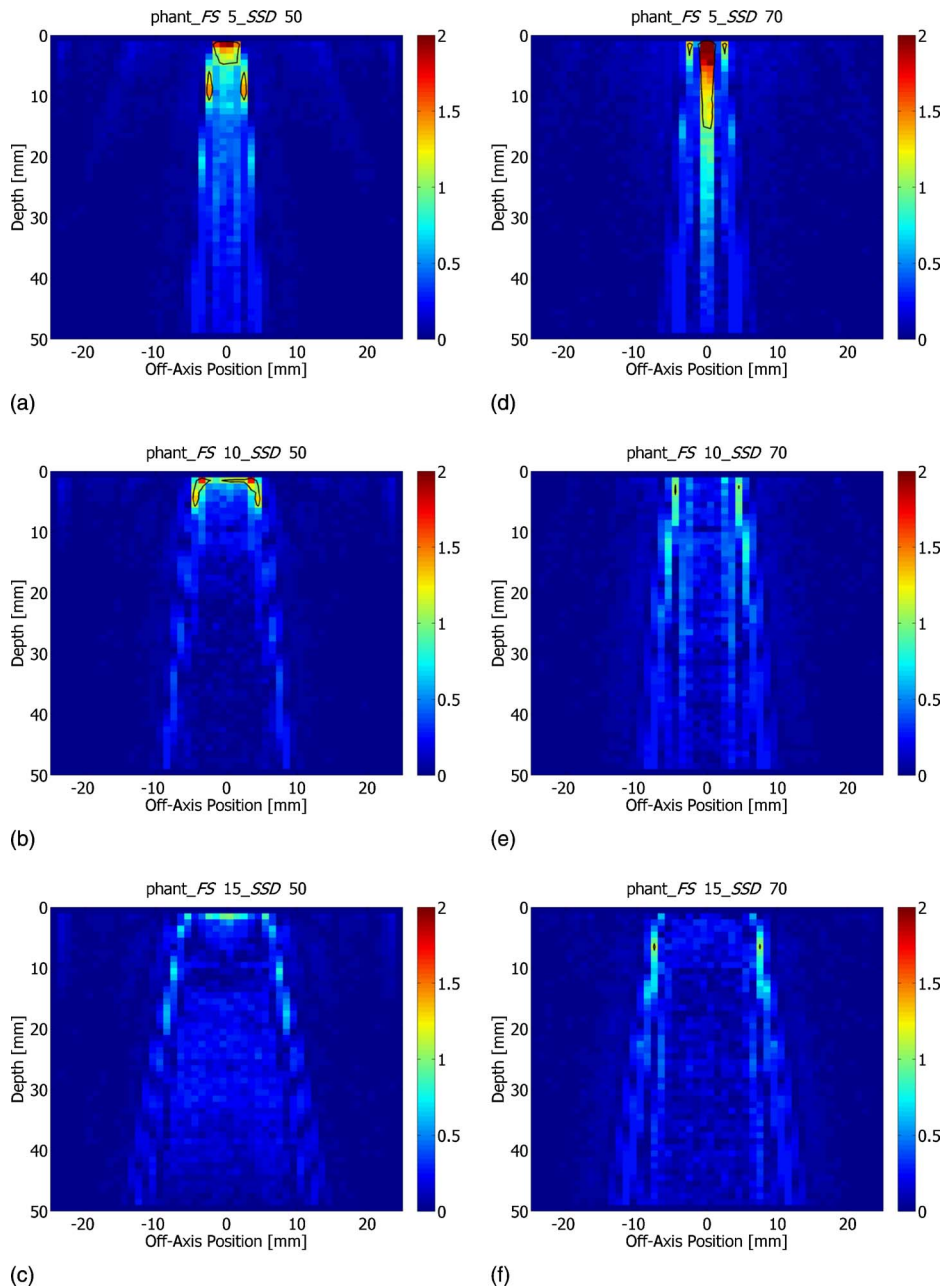
FIG. 13. Comparison of the model with the gamma dose distribution method. The distance and dose difference criteria were 1 mm and 5%, respectively. A contour is drawn where $\gamma = 1$. Left column: dose differences for SSD=50 mm and FS= (a) 5, (b) 10, and (c) 15 mm. Right column: dose differences for SSD=70 mm and FS= (d) 5, (e) 10, and (f) 15 mm.

the extrapolated results have to be taken with caution as the magnitudes of errors associated with extrapolation are difficult to estimate without Monte Carlo simulation or actual measurements. Comparison of the model with the Monte Carlo simulations, as well as independent comparison using the gamma dose distribution method, showed that the variations are within 5% error for field sizes larger than 10 mm, and up to 10% for smaller field sizes in shallow phantom regions. The overall difference between the Monte Carlo data and the data predicted by Eq. (1) could be improved by using higher-order terms for fitting depth and field size dependences of the parameters of radial distribution function. This

is especially evident in Fig. 11 where 2D functional dependence of fit parameters on depth and field size is shown. The corresponding surface fits are quite flat, whereas the "real" nature of the parameter behavior is fairly wavelike in certain regions. Higher-order modeling of such regions would minimize current deviations between the model and the simulations.

The future goals include modeling of a high dose-rate ^{192}Ir source that is being clinically used for treating human subjects. Such an approach will have smaller SSDs than the current model. These beam models will be used to plan radiation therapy in small animals using a microRT device.

[1] D. Zhao, A. Constantinescu, C. H. Chang, E. W. Hahn, and R. P. Mason, "Correlation of tumor oxygen dynamics with radiation response of the dunning prostate R3327-HI tumor," Radiat. Res. **159**, 621–631 (2003).

[2] H. L. Guo, D. Wolfe, M. W. Epperly, S. Huang, K. Liu, J. C. Glorioso, J. Greenberger, and D. Blumberg, "Gene transfer of human manganese superoxide dismutase protects small intestinal villi from radiation injury," J. Gastrointest Surg. **7**, 229–235 (2003).

[3] M. A. Khan, J. Van_Dyk, I. W. Yeung, and R. P. Hill, "Partial volume rat lung irradiation; assessment of early DNA damage in different lung regions and effect of radical scavengers," Radiother. Oncol. **66**, 95–102 (2003).

[4] M. A. Khan, R. P. Hill, and J. Van_Dyk, "Partial volume rat lung irradiation: an evaluation of early DNA damage," Int. J. Radiat. Oncol., Biol., Phys. **40**, 467–476 (1998).

[5] C. DesRosiers, M. S. Mendonca, C. Tyree, V. Moskvin, M. Bank, L. Massaro, R. M. Bigsby, A. Caperell-Grant, S. Valluri, J. R. Dynlacht, and R. Timmerman, "Use of the Leksell gamma knife for localized small field lens irradiation in rodents," Technol. Cancer Res. Treat. **2**, 449–454 (2003).

[6] B. Duchemin and N. Coursol, "Reevalution de l' ^{192}Ir," Technical Note LPRI/93/018, DAMRI (CEA, France, 1993).

[7] D. A. Low, M. Vicic, S. Mutic, J. O. Deasy, A. Hope, D. J. Robertson, and P. W. Grigsby, "Prototype design of a microRT irradiator Proceedings of the 14th International Conference on the Use of Computers in Radiation Therapy, Seoul, Korea," 2004.

[8] D. W. O. Rogers, B. Walters, and I. Kawrakow, NRCC Report No. PIRS-0509(A)revI (2004).

[9] I. Kawrakow and D. W. O. Rogers, Technical Report PIRS-701 (2000).

[10] F. M. Khan, *The Physics of Radiation Therapy*, 3rd ed. (Lippincott Williams & Wilkins, Philadelphia, PA, 2003).

[11] D. A. Low and J. F. Dempsey, "Evaluation of the gamma dose distribution comparison method," Med. Phys. **30**, 2455–2464 (2003).

[12] J. F. Dempsey, D. A. Low, S. Mutic, J. Markman, A. S. Kirov, G. H. Nussbaum, and J. F. Williamson, "Validation of a precision radiochromic film dosimetry system for quantitative two-dimensional imaging of acute exposure dose distributions," Med. Phys. **27**, 2462–2475 (2000).

[13] M. J. Berger, J. H. Hubbell, S. M. Seltzer, J. Chang, J. S. Coursey, R. Sukumar, and D. S. Zucker, XCOM: Photon Cross Section Database (version 1.3), available at http://physics.nist.gov/xcom, National Institute of Standards and Technology, Gaithersburg, MD (2005).